Highly Consistent Brightness Temperature Fundamental Climate Data Record From SSM/I and SSMIS

Shi Liu, Banghai Wu, Cheng-Zhi Zou, and Yu Wang

***Abstract*— A continuous and consistent fundamental climate data record (FCDR) from satellite observations is an essential source for climate research. In this study, a highly consistent multichannel brightness temperature (TB) FCDR during 1991–present has been developed using measurements from two Special Sensor Microwave Imagers (SSM/I) onboard F11 and F13 satellites and one Special Sensor Microwave Imager/Sounder (SSMIS) onboard F17 satellite from the U.S. Defense Meteorological Satellite Program (DMSP). The hardware differences between these instruments were corrected by a combination of several technologies including the principal component analysis (PCA), use of the third instrument as an intermediate, and the weighted average approach which takes into account interchannel covariability and observation matchup issues. After intercalibration, all imagers were homogenized with SSMIS, which was used as an observation reference. The mean biases of the recalibrated TBs for almost all channels between any two instruments are less than 0.2 K globally with the standard deviations (STDs) less than 1.2 K. This resulted in a 30-year long continuous and stable FCDR. Based on this FCDR, a long time series of column water vapor (CWV) over the global oceans was retrieved. Validation of this retrieved moisture product against reanalysis data and site measurements from radiosonde and Global Navigation Satellite System (GNSS) resulted in reasonably good accuracy, suggesting that the presented FCDR has high application potential for climate research.**

***Index Terms*— Fundamental climate data record (FCDR), intercalibration, Special Sensor Microwave Imager/Sounder (SSMIS), Special Sensor Microwave Imagers (SSM/I).**

Manuscript received 29 March 2023; revised 10 August 2023 and 10 September 2023; accepted 13 September 2023. Date of publication 18 September 2023; date of current version 9 October 2023. This work was supported in part by the National Natural Science Foundation of China under Grant 41875024 and Grant 42075124, in part by the Ministry of Science and Technology of China under Grant 2022YFC3104303, in part by the FY Satellite Advanced Planning under Grant FY-APP-ZX-2022.0212, in part by the Fundamental Research Funds for the Central Universities, and in part by the Jiangsu Provincial 2011 Program (Collaborative Innovation Center of Climate Change). *(Corresponding author: Yu Wang.)*

Shi Liu and Banghai Wu are with the School of Earth and Space Sciences, University of Science and Technology of China, Hefei 230026, China (e-mail: ls1996@mail.ustc.edu.cn).

Cheng-Zhi Zou is with the Center for Satellite Applications and Research, National Oceanic and Atmospheric Administration (NOAA)/National Environmental Satellite, Data, and Information Service (NESDIS), College Park, MD 20740 USA (e-mail: cheng-zhi.zou@noaa.gov).

Yu Wang is with the School of Earth and Space Sciences and the Hefei National Laboratory, University of Science and Technology of China, Hefei 230026, China, and also with the Chinese Academy of Sciences (CAS) Center for Excellence in Comparative Planetology, Hefei 230026, China (e-mail: wangyu09@ustc.edu.cn).

Digital Object Identifier 10.1109/TGRS.2023.3316694

I. Introduction

THE spaceborne passive microwave (PMW) remote sensing technology has been widely applied to obtain the physical parameters related to the water and energy cycles of the Earth system owing to its unique advantage of all-sky measurements, including during night and with cloud cover [1], [2], [3], [4]. As outstanding representatives of PMW radiometers, the Special Sensor Microwave Imager (SSM/I) and its successor, the Special Sensor Microwave Imager/Sounder (SSMIS), have been flown on board a set of polar-orbiting satellites (F08–F19) under the Defense Meteorological Satellite Program (DMSP) from the United States Department of Defense [5], [6], [7], [8]. Since the 1990s, measurements from these sensors, i.e., brightness temperatures (TBs) on multiple microwave channels, have been used to retrieve a diverse range of atmospheric variables such as rainfall rate, water vapor content, cloud liquid water [9], [10], [11], [12], [13], [14], [15], [16], [17], and surface parameters such as sea surface wind speed, sea surface temperature, and so on [18], [19], [20], [21], [22].

Although continuous observations of multiple DMSP satellites had spanned for decades, any single satellite among them lasted for only a few years. For the SSM/I series to be useful for climate change research, intersensor calibration of multisatellites is required to establish long-term consistent TB observations, the so-called fundamental climate data records (FCDRs). Several intercalibration studies for the SSM/I and SSMIS instruments onboard different satellites had been conducted in past years. Colton and Poe [23] statistically compared the monthly averages of TBs from different SSM/I's on F08 to F14 satellites. Yang et al. [24] carried out SSM/I intersensor calibration using a simultaneous conical overpass (SCO) method. This method searched for "simultaneous" observation samples defined within a small temporal interval and spatial distance from different PMW conical sensors. Such SCOs do not contain diurnal drifting errors between satellite pairs, as a result, they are ideal for intersatellite calibration to identify sensor calibration biases. Sapiano et al. [25] developed a TB FCDR from six SSM/I's based on a similar SCO technique, as well as the vicarious cold reference (VCR) method [26] and double differencing method. Especially, the Global Precipitation Measurement (GPM) Intersatellite Calibration (X-CAL) Working Group recalibrated the GPM constellation radiometers including multiple SSM/I and SSMIS sensors with various techniques [27]. The group also developed a set of

© 2023 The Authors. This work is licensed under a Creative Commons Attribution-NonCommercial-NoDerivatives 4.0 License.
For more information, see https://creativecommons.org/licenses/by-nc-nd/4.0/

homogenized TB data in which the GPM Microwave Imager was used as a reference. In addition, several other working groups had also developed long-term TB FCDR from multiple SSM/I and SSMIS observations, starting with calibration of the antenna temperature [28], [29] and the raw Earth counts [30], respectively.

Essentially, intersensor TB biases can be divided into those from calibration and hardware. Calibration biases are due to discrepancies in data preprocessing, prelaunch, and on-orbit correction approaches. On the other hand, hardware differences include those in channel frequency, Earth incident angle, bandwidth, and so on [31]. It is noted that research work as mentioned above emphasized the correction of calibration biases more than the hardware differences. Hardware differences incurred for SSM/I and SSMIS in changes of high frequency channels from 85.5 to 91.655 GHz, as well as reduction of bandwidth and noise equivalent differential temperature for all channels [5], [6], [7], [32]. Without adjustment of hardware differences, the TBs from these sensors are still not entirely consistent even after recalibration. Furthermore, unremoved intersensor TB biases would be transferred to thematic climate data record (CDR) through parameter retrievals [33], limiting its applications in climate change research. Several studies have attempted to homogenize SSM/I with SSMIS over the polar regions using the SCO matchups by methods such as simple linear TB corrections for snow depth or sea ice retrievals [34], [35], [36], [37], [38], [39]. In these studies, the correction for instruments was usually performed channel by channel without consideration of the covariability between channels.

Given the natural variability in surface conditions, it is physically more sound to jointly adjust the emissivity vector composed of multiple channels rather than TBs channel-by-channel since emissivities at typical microwave window frequencies between 10 and 85 GHz are correlated [40]. Recently, Wu et al. [31] used the principal component analysis (PCA) method with incorporation of interchannel covariance to remove the hardware biases between different instruments after correction of calibration deviations. In their study, by using the Advanced Microwave Scanning Radiometer-2 onboard the JAXA's Global Change Observation Mission 1st-Water satellite as a reference, measurements from the Microwave Radiation Imager onboard the Chinese Feng Yun-3B satellite and the Advanced Microwave Scanning Radiometer for Earth Observing System (EOS) equipped on the NASA Aqua satellite were homogenized. Intersensor biases were less than 1 K for the three satellites after hardware differences were removed. However, the TB FCDR in Wu's study is only 20 years long (since 2002) which is still short for climate change research. In this study, we attempt to use a similar PCA technology, as well as several other techniques, to homogenize SSM/I and SSMIS sensors with a focus on correction of hardware biases, and then to develop a set of highly consistent multichannel global TB FCDR for a period of up to 30 years.

To develop TB FCDR with high consistency from the SSM/I and SSMIS instruments, we only select a subset of satellites from the DMSP series. Two criteria are used in the satellite selection. The first is to ensure that the entire observations

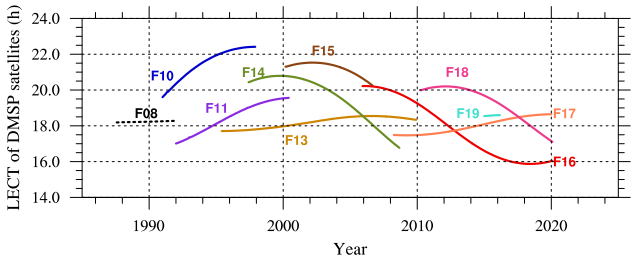

Fig. 1. LECT of the ascending orbits for DMSP satellites, except that F08 (dashed line) shows descending LECT.

of the selected sensors have no temporal gap from 1991 to present. Second, orbital drifts of the chosen satellites should be minimal and the local observation times, represented by the local equator crossing times (LECTs), between sensors should be close to each other to avoid diurnal sampling biases in TB. We found that a combination of F11, F13, and F17 best meets the above criteria. As shown in Fig. 1 and Table I, the temporal coverage of F11 was from 1991 to 2000, F13 from 1995 to 2009, and F17 from 2006 to present, respectively. The operational periods of these satellites allow sufficient overlaps and observation matchups for intersensor calibration. Furthermore, they have similar LECTs near 18:00 for the ascending node, except that F11 drifted for 3 h from 17:00 to 20:00 throughout its lifecycle. Thus, in this study, only observations of the radiometers on these three satellites are recalibrated and further combined to construct TB FCDR. For potential extension of the FCDR to future satellites, the two earlier SSM/I's are intercalibrated to the later SSMIS which is still in orbit. Since SSM/I does not have sounding channels as in SSMIS, our FCDR development only includes seven imaging channels consisting of 19.35, 37.0, and 91.655 GHz (referred to as 19, 37, and 91 GHz hereafter) with both vertical (V) and horizontal (H) polarizations, and 22.235 GHz (referred to as 22 GHz) with only vertical polarization.

The rest of this article is organized as follows. Section II introduces the satellite data and its preprocessing method used in this study. Section III describes in detail the intercalibration between different sensors. Section IV describes the performance of the developed TB FCDR from multisensor observations and an example of its application in obtaining long-term water vapor products. Section V gives a conclusion.

II. Data and Preprocessing

The GPM Common Calibrated TBs Collocated L1C datasets from the X-CAL [41] is used in this study, which includes L1C SSM/I (Version 6) on F11 [42] and F13 [43] and L1C SSMIS (Version 5) on F17 [44]. It is worth mentioning that the F17 SSMIS data from the X-CAL starts from March 2008, rather than its launch time in December 2006. The X-CAL calibration involved multiple independent approaches. Specifically, the SSM/I and SSMIS TBs for all channels were adjusted via piecewise linear functions constrained with specified anchor points, reorbitization, and quality control procedures (Algorithm Theoretical Basis Document, https://arthurhou.pps.eosdis.nasa.gov/Documents/L1C_ATBD.pdf). These recalibrated TB data

TABLE I
MAIN CHARACTERISTICS OF THE PMW IMAGERS WITH IMAGING CHANNELS USED IN THIS STUDY (V AND H REPRESENT VERTICAL AND HORIZONTAL POLARIZATION, RESPECTIVELY)

Platform	Instrument	LECT (h)	Start time	Stop time	Frequency (GHz)
DMSP F11	SSM/I	17:00-20:00 ascend	Dec 1991	May 2000	19.35 (V, H), 22.235 (V), 37.0 (V, H), 85.5 (V, H)
DMSP F13	SSM/I	17:51-18:51 ascend	May 1995	Nov 2009	19.35 (V, H), 22.235 (V), 37.0 (V, H), 85.5 (V, H)
DMSP F17	SSMIS	18:40-19:40 ascend	Dec 2006	Present	19.35 (V, H), 22.235 (V), 37.0 (V, H), 91.655 (V, H)
TRMM	TMI	Non-Sun-synchronous	Dec 1997	Apr 2015	19.35 (V, H), 21.3 (V), 37.0 (V, H), 85.5 (V, H)

were broadly used in geophysical studies. For example, Sharifnezhad et al. [45] investigated diurnal cycles of the recalibrated TBs over land on a global scale. Lee et al. [46] retrieved and studied the long-term Arctic Snow/Ice interface temperature. Liu et al. [47] calculated near-surface winds, humidity, and temperature over the ocean to investigate the relationship between freshwater flux and sea surface salinity. Although with these studies, however, the hardware differences in the X-CAL TB still remained. To make the X-CAL TB a FCDR dataset, these hardware differences must be removed. This is the primary purpose of our study here. Note that the SSMIS 37V TB data has been flagged as "missing" from April 2016 to May 2016 and from August 2016 to present due to sensor issues. As a result, for consistency, the climatological analysis for TBs on multiple channels and relevant retrievals are performed only up to the end of year 2015 in Section IV, although TBs for other channels are available up to the present.

For intercalibration purposes, SCO matchups between satellite pairs were collected using criteria similar to Wu et al. [31] and Yang et al. [48], where spatial distances and temporal intervals should be less than 5 km and 10 min, respectively. A clear sky filter [49], [50] was applied over the oceanic SCOs for alleviating disturbances from clouds to subsequent PCA procedures. For SCOs over land, no clear sky filter was applied as clouds have less impact on microwave signals there, especially at low frequencies. For DMSP polar-orbiting satellites, SCO pairs can only be collected near the Polar regions. It should be noted that significant differences exist in TB values for each channel, and in interchannel covariability between the polar and the tropical (and also the subtropical) areas, due to large differences in sensor responses to different amounts of column water vapor (CWV) and other hydrological variables. Consequently, the polar SCO samples are unsuitable for global PCA analysis. To overcome this limitation, another microwave imager from a non-Sun-synchronous satellite, the Tropical Rainfall Measuring Mission (TRMM) Microwave Imager (TMI), is used as a bridge instrument to pair separately with these three different DMSP sensors in low latitudinal areas (within 40 °N and 40 °S) determined by the inclination angle of TMI. As shown in Table I, TMI and DMSP sensors (especially SSM/I) have similar frequencies and channels. This allows TB intercalibrations on all channels. To avoid potential uncertainties in PCA analysis due to inconsistency of calibration methods between TMI and the DMSP imagers, the recalibrated TMI TB dataset (Version 5) also from the X-CAL [51], rather than the original observation product, is utilized for the period from 1998 to 2014.

TABLE II
RECLASSIFICATION OF 17 LAND COVER TYPES FROM IGBP (EXCEPT WATER BODY AND SEA ICE)

Combined Land cover type	IGBP's 17 Land cover types
Forestry	Evergreen Needleleaf Forest Evergreen Broadleaf Forest Deciduous Needleleaf Forest Deciduous Broadleaf Forest Mixed Forest Closed Shrublands Open Shrublands
Grasslands	Woody Savannas Savannas Grasslands Permanent Wetlands Croplands Urban and Built-Up Cropland/Natural Vegetation Mosaic
Ice on land	Permanent Snow and Ice
Others	Barren or Sparsely Vegetated Unclassified

In addition to SCOs, the PCA method requires detailed land cover classifications for better TB reconstruction. Wu et al. [31] used 17 land cover types from the International Geosphere–Biosphere Program (IGBP) Land Cover Type Classification product [52] (see Table II). Here, the IGBP land cover data were derived from the Moderate Resolution Imaging Spectroradiometer (MODIS) Land Cover Climate Modeling Grid (MCD12C1) Version 6 data product [53]. However, we found that several surface types have similar radiative properties which can be regrouped for simplification (see Table II). As an example, the urban and built-up land types cannot be separated from the grassland type in our land type regrouping processes owing to their similar radiative characteristics. Therefore, only four combined land types including forestry, grassland, ice on land, and the rest as "others" are used in this study. With ocean and sea ice, a total of six surface types are defined for each $0.05^\circ \times 0.05^\circ$ grid globally. In actual applications, only grids with more than 80% of the area falling in the same surface type are selected for subsequent PCA analysis. Other grids with more complex land cover are discarded. It should be noted that the MCD12C1 dataset only covers the time period from 2001 to 2020. During this 20 year of period, only 2.3‰ of the global grids was found to incur changes in land cover types in our data quality examination. This suggested that the land type changes over time is ignorable during the period of interest in our study. As a result, the land cover classification in 2001 is used for

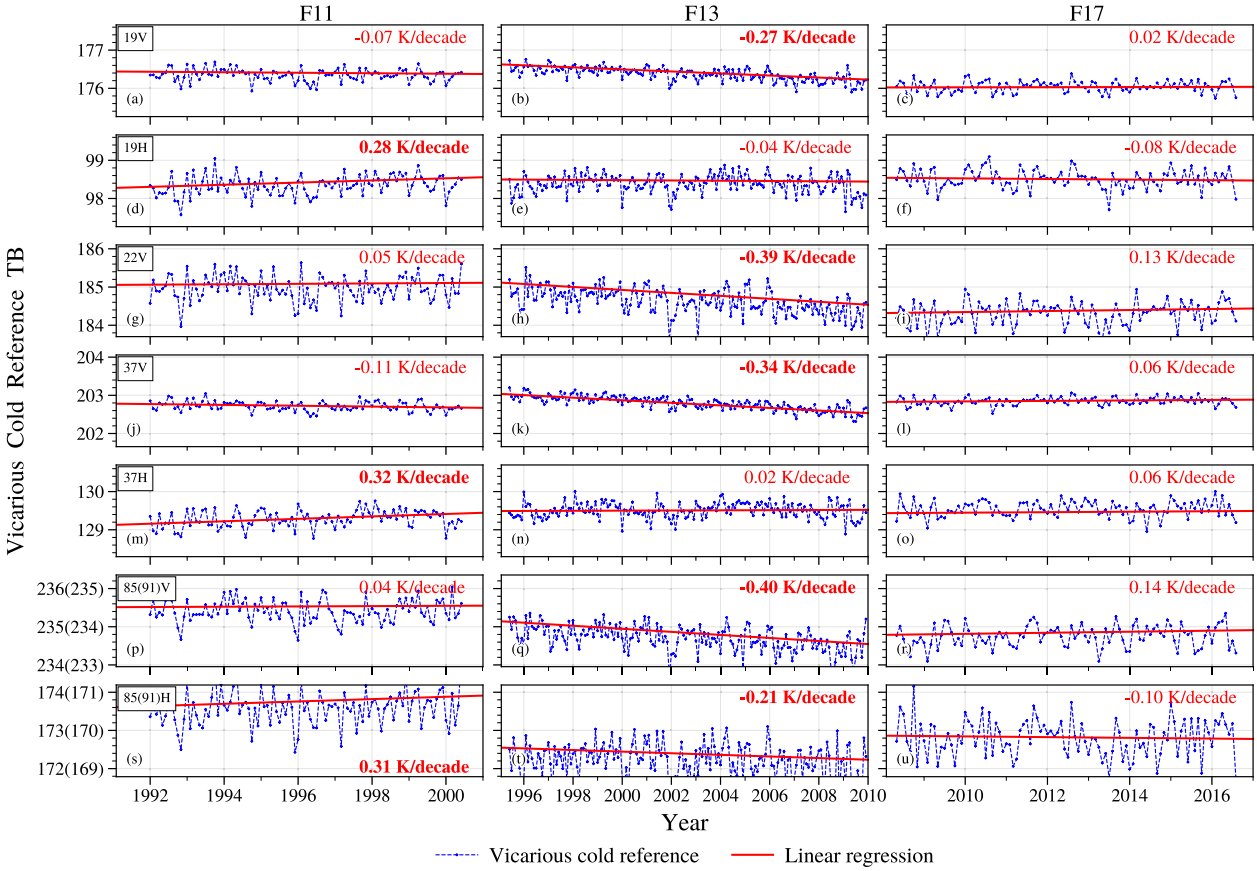

Fig. 2. Time series of the VCR for window channels from (top) 19 GHz V to (bottom) 85/91 GHz H on (left) F11, (middle) F13, and (right) F17. The solid red lines represent the linear regression trends. Trends with statistical significance in the Mann-Kendall test are highlighted with bold texts. (a), (b) and (c) 19V, (d), (e) and (f) 19H, (g), (h) and (i) 22V, (j), (k) and (l) 37V, (m), (n) and (o) 37H, (p), (q) and (r) 85/91V, and (s), (t) and (u) 85/91H.

the period from 1991 to 2000. For the F17 data after 2021, land cover type information is not needed as F17 serves as the reference and requires no recalibration.

The instantaneous fields of view (IFOVs) of SSM/I and SSMIS are different for different channels with smaller IFOVs for higher frequencies. The 19-GHz channels of SSMIS and SSM/I exhibit averaged cross-scan and along-scan sizes approximately 70 and 42 km, respectively, compared to 15 × 13 km in the 85-/91-GHz channels. These pixel sizes are determined by the distances between scan points which are about 25.0 × 12.5 km for low-frequency channels and 12.5 × 12.5 km for high-frequency channels (85/91 GHz) in L1C datasets. With its 1700-km swath and nearly 90° orbital inclination, the SSMIS instrument provides daily global observations with gaps near the equator. However, seamless global coverage without gaps can be achieved with three successive days of observations. The SSM/I have a narrower swath of 1400 km and similar orbital inclination and it provides global observations in daily mapping with gaps in midlatitudes. Global coverage without gaps for the SSM/I observations can be achieved for data collected over an entire week. The TMI instrument has a swath width of 760 km and a spatial resolution of 7 × 5 km to 63 × 37 km, depending on the channel frequencies (highest resolution at 85 GHz). The TMI pixel sizes are about 13.7 × 9.2 km for all low-frequency channels and 13.7 × 4.6 km for the 85-GHz channel in TMI TB product. It is worth noting that that the TRMM orbit was boosted from an altitude of 350 to 402.5 km in 2001. This had caused the resolution of TMI slightly decreased [54]. Given the above different IFOV sizes and for consistency in intercalibration, we resampled the high-frequency data to make their pixel sizes align with the low-frequency channels. The resulting FCDR after intercalibration also maintains the consistent resolution of 25.0 × 12.5 km with the low-frequency channels.

Before conducting intercalibration among different instruments, possible TB drifts in L1C dataset were first checked and corrected based on the VCR approach by Ruf [26], Kroodsma et al. [55], and Xie et al. [56]. In this method, the minimum TB at cold point over the open ocean at any microwave channel is always correlated with a fixed sea surface temperature with low water vapor content. Such a minimum TB is statistically almost invariant. As such, any large annual variation of the minimum TB should be considered as radiometer calibration drift over time. Fig. 2 gives time series of the monthly VCR TBs on all the seven imaging channels for the three SSM/I and SSMIS sensors, respectively. It is seen that cooling drifts occurred on almost all channels on the F13 SSM/I, except for channel 37H, with the largest drift up to −0.4 K/decade. In addition, there is a warm drift for the SSM/I channel 37H and 85H on F11 with a value approximately 0.3 K/decade. Compared to SSM/I's, the SSMIS on F17 is more stable,

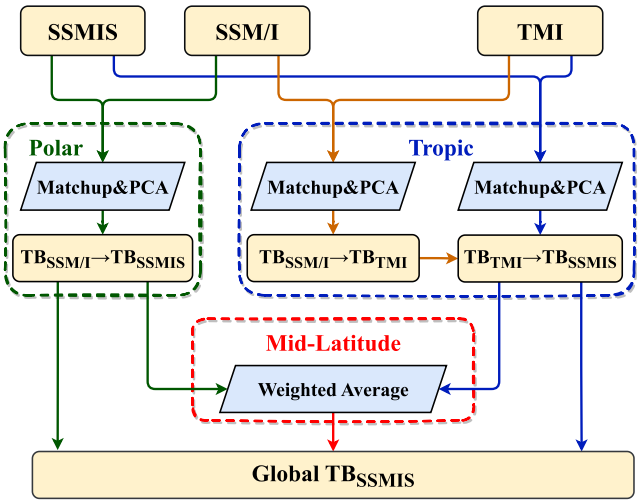

Fig. 3. Flow diagram of TB intercalibration between SSM/I on F13 and SSMIS on F17.

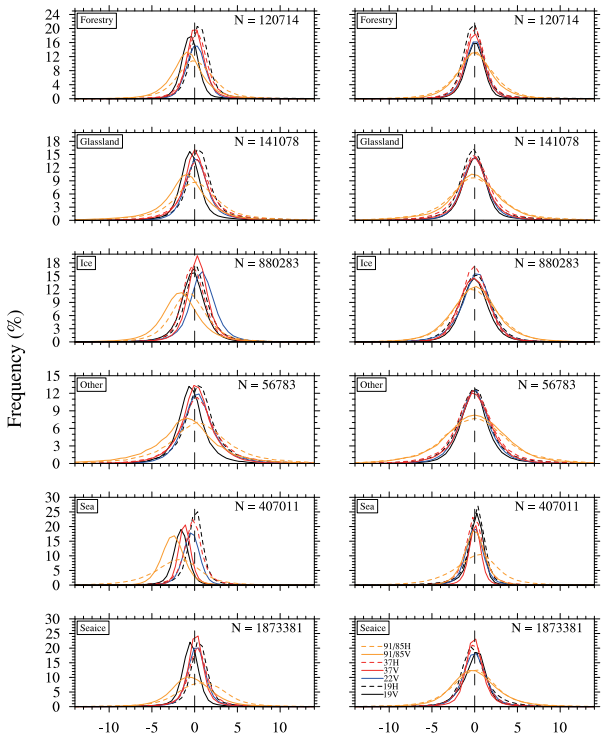

Fig. 4. PDF distribution of TB biases for SCO matchups of SSM/I on F13 and SSMIS on F17 (left) before and (right) after intercalibration over the Polar regions. Figures from the top to the bottom show pdfs with different land cover types: forestry, grassland, ice on land, other, waterbody, and sea ice, respectively. The vertical black dash lines indicate the unbiased 0 lines.

except that the 22V and 91V channels exhibited a small warm drift. These drifts occurred most likely caused by calibration errors. In developing satellite-based temperature CDR, Zou et al. [57] suggested that degradations over time in emissivity of blackbody warm target, reflector, antenna surface materials, and instrument calibration nonlinearity could cause calibration drifts during conversions from raw counts data to radiance (or TBs) in satellite microwave sounder observations. These mechanisms could also be applied here to explain the calibration drifts in observations from the microwave imagers. These drifts could affect the FCDR consistency and the subsequent retrieval of atmospheric parameters. For example, the sensitivity of the CWV to TB on the 22V absorbing channel may reach as high as 2.5 $\mathrm{kg\,m^{-2}\,K^{-1}}$. As a result, a TB drift on the order of 0.4 K/decade would cause a spurious CWV trend of 1.0 $\mathrm{kg\,m^{-2}}$ per decade. As part of preprocessing before intercalibration, TB drifts on each channel were removed by subtracting a linear trend from the original TBs [31] in this study.

III. Intercalibration

A. Adjustment of F13 SSM/I

We use F17 SSMIS as a reference for the F13 SSM/I calibration. With this reference, F13 can be intercalibrated directly using their overlaps. Fig. 3 schematically shows the intercalibration strategy for the F13 SSM/I. Basically, the adjustment process is divided into three geographical regions: the polar (beyond 65 °S or 65 °N), the tropical and subtropical (40 °S–40 °N), and the midlatitudinal (between 40 °N and 65 °N and between 40 °S and 65 °S) regions.

In the Polar regions, the SSM/I TBs are converted to SSMIS-equivalent using the PCA technology [31]. In this method, the SSMIS TBs in the SSM/I-SSMIS SCO pairs are first decomposed into seven principal components (PCs) for their seven channels. But in fact, the first four PCs had already explained 99.5% of the total variance. Consequently, PC coefficients representing the relationship between these four PCs and the F13 SSM/I TBs on all channels in the SCO pairs are calculated through multiple linear regressions. Then, the corresponding SSM/I PCs are obtained by applying these coefficients to all SSM/I observations over the Polar regions. Finally, these PCs are reconstructed to generate the SSMIS-equivalent TBs from SSM/I.

Fig. 4 compares the Gaussian-shape probability density function (pdf) distributions of TB differences between SSM/I and SSMIS in their SCO pairs before and after the PCA corrections for all channels and for various surface types over the Polar regions. Typically, the spreads in biases are larger for channels with higher frequency. Before adjustment, the mean biases between the two sensors vary from −3 to 1 K, depending on channel frequencies and polarizations (left). These larger biases are mostly caused by hardware differences in the X-CAL datasets. This can be seen from the SSMIS 91-GHz and SSM/I 85-GHz SCO pairs. These pairs have different channel frequencies and show larger mean biases with larger bias spread than other channels with the same channel frequencies. After the PCA correction (right), an unbiased Gaussian distribution with a mean difference close to 0 K was obtained for all channels regardless of surface types, suggesting that the hardware differences between the two sensors are largely eliminated.

In the tropical and subtropical regions, the same PCA method is adopted, except that TMI is used as an intermediate reference for converting F13/SSM/I to F17/SSMIS using their respective matchups. The pdf distributions of TB differences between TMI and the two DMSP sensors are similar to that in the Polar regions (not shown), except that the 22V channel has

a mean bias peaking far from the center (about −8 K) over the ocean before correction. This occurred most likely because the frequency difference in the absorbing channels between TMI and DMSP sensors (21.3 versus 22.235 GHz) leads to larger TB differences in response to higher water vapor content in the tropics. Note that measurements from the water vapor channel have been involved in many retrieval algorithms, either to obtain CWV or conversely to remove its effect from retrievals of other atmospheric and surface variables [4]. Therefore, the importance of consistent observations on the water vapor channel cannot be overemphasized. Here, the PCA technique is used to effectively correct the hardware difference of water vapor channels between instruments, resulting in a mean bias under 0.2 K. This makes it possible to establish a continuous and consistent CWV CDR based on a unified retrieval algorithm later on.

In the midlatitudes, there are no SCOs for any pairs among SSM/I, SSMIS, and TMI. As such, relationships between SSM/I and SSMIS obtained above in the polar and tropical/subtropical regions are modified for midlatitudinal TB transformation. We test three approaches: 1) extending the polar conversion relationship to the midlatitude regions; 2) extending the tropical/subtropical conversion relationship to the midlatitude regions; and 3) extending both the polar and tropical/subtropical relationships to the midlatitude regions based on a weighted average of their latitudinal distance to the conversion point. Fig. 5 shows latitudinal distribution of the SSM/I TB differences relative to SSMIS during 2009 for all channels calculated based on these different transformation relationships over the global ocean and land. It is seen that the uncorrected SSM/I TB biases in nonpolar regions over the ocean exceed 1 K in low-frequency channels and are much larger than 2 K in high-frequency channels. After correction, TB biases were reduced to near 0 K in both the polar and tropical/subtropical regions. This is consistent with the pdf distribution shown in Fig. 4. Over the Southern midlatitude oceans, TB biases progressively increase equatorward from 0 to 1 K for low-frequency channels and decrease to −1 K for 85-/91-GHz channels when the polar TB conversion relationship is used to correct the SSM/I observations. Similarly, TB biases increase from close to 0-K poleward over the Southern midlatitude oceans for low-frequency channels when the tropical correction relationship is used for the midlatitudes. These phenomena suggest that neither polar nor tropical/subtropical TB corrections can be directly adopted in the midlatitudes. In fact, because the TB magnitudes on each channel and interchannel correlations vary with latitude due to latitudinal-dependency in the physical variables (such as sea surface temperature) that the channel measures, the calculated PCs and their corresponding coefficients are latitude-dependent in the PCA analysis. This is also the reason for the smaller TB biases in the midlatitude regions at latitudes closer to the polar region when the polar correction relationship is used. Similarly, the tropical/subtropical correction relationship is more applicable in lower latitudes within the midlatitude regions. Considering these limitations of either the polar or the tropical/subtropical correction relationships, we used the distance-weighted averaging approach to correct SSM/I TBs over the midlatitude regions for ocean and land, respectively. Specifically, the corrections at any point in the midlatitudinal regions are a linear interpolation between those at the internal boundaries of the polar regions (65 °N or 65 °S) and external boundaries of the tropical/subtropical regions (40 °N or 40 °S) with their latitudinal distances to the midlatitudinal point as the weighting. The SSM/I TB biases derived using this approach were reduced to near 0 K in the Northern midlatitude oceans (see Fig. 5). However, TB biases in the Southern midlatitudinal oceans are still slightly larger, especially for the 19V and 89V channels [see Fig. 5(a) and (k)]. One possible reason for this is the influence of the predominant strong westerly winds over this region. Because there are no samples with wind speeds exceeding 8.5 m/s in the PCA analysis, either from the tropical or polar regions, the applicability of the correction method would be affected in the high wind speed regions. In contrast, TB biases over land were near 0 K after correction in nearly all latitudes except with a bias about 0.5 K near 40 °N. This is likely attributed to the complex topography of Tibetan Plateau that would exhibit complicated microwave emission and scattering properties. Note that the longitudinal length of a fixed-angle rectangle decreases as the pixel goes from the equator toward the poles. But, this does not affect the geographic weighting methods proposed here because the extension of the tropical/subtropical or polar transformation relationships to the midlatitudes is only a function of latitudinal distance.

TABLE III

MEAN TB BIASES AND STDS BETWEEN F13 SSM/I AND F17 SSMIS BEFORE (UNCAL) AND AFTER (CAL) INTERCALIBRATION FOR THE PERIOD FROM OCTOBER 2008 TO SEPTEMBER 2009 OVER OCEAN AND LAND, RESPECTIVELY

Channel [GHz]	Oceans		Lands	
	Mean[K] Uncal/Cal	STD[K] Uncal/Cal	Mean[K] Uncal/Cal	STD[K] Uncal/Cal
19.35V	1.50/-0.05	0.69/0.72	0.52/-0.14	0.58/0.88
19.35H	0.41/-0.04	1.02/0.80	-0.36/-0.02	0.84/1.17
22.235V	0.59/-0.17	0.75/1.06	-0.17/-0.14	0.85/0.86
37.0V	0.99/0.05	0.68/0.49	0.12/0.05	0.64/0.81
37.0H	0.36/0.16	0.71/0.75	-0.08/-0.15	0.82/0.73
85.5/91.655V	2.70/-0.11	1.18/0.75	0.93/-0.16	0.80/1.15
85.5/91.655H	3.85/0.23	2.51/0.80	0.42/-0.23	0.99/1.17

The steps detailed above effectively converted SSM/I TBs to SSMIS globally. After this conversion, the overall intercalibration results were examined. Fig. 6 illustrates the global distribution of TB differences between F17 SSMIS and F13 SSM/I, both before and after intercalibration, for all channels during their one-year overlaps from October 2008 to September 2009. Before correction [see Fig. 6 (left)], warm biases in TBs are evident in channels 19V, 91V, and 91H with values exceeding 2 K over the ocean. After correction, biases are typically less than 1 K across most areas for all channels [more than 80% of the global 1° × 1° grids, Fig. 6 (right)], regardless of the surface types. However, biases over the polar coastal areas were slightly larger possibly due to the complex influence of sea ice and land ice on microwave

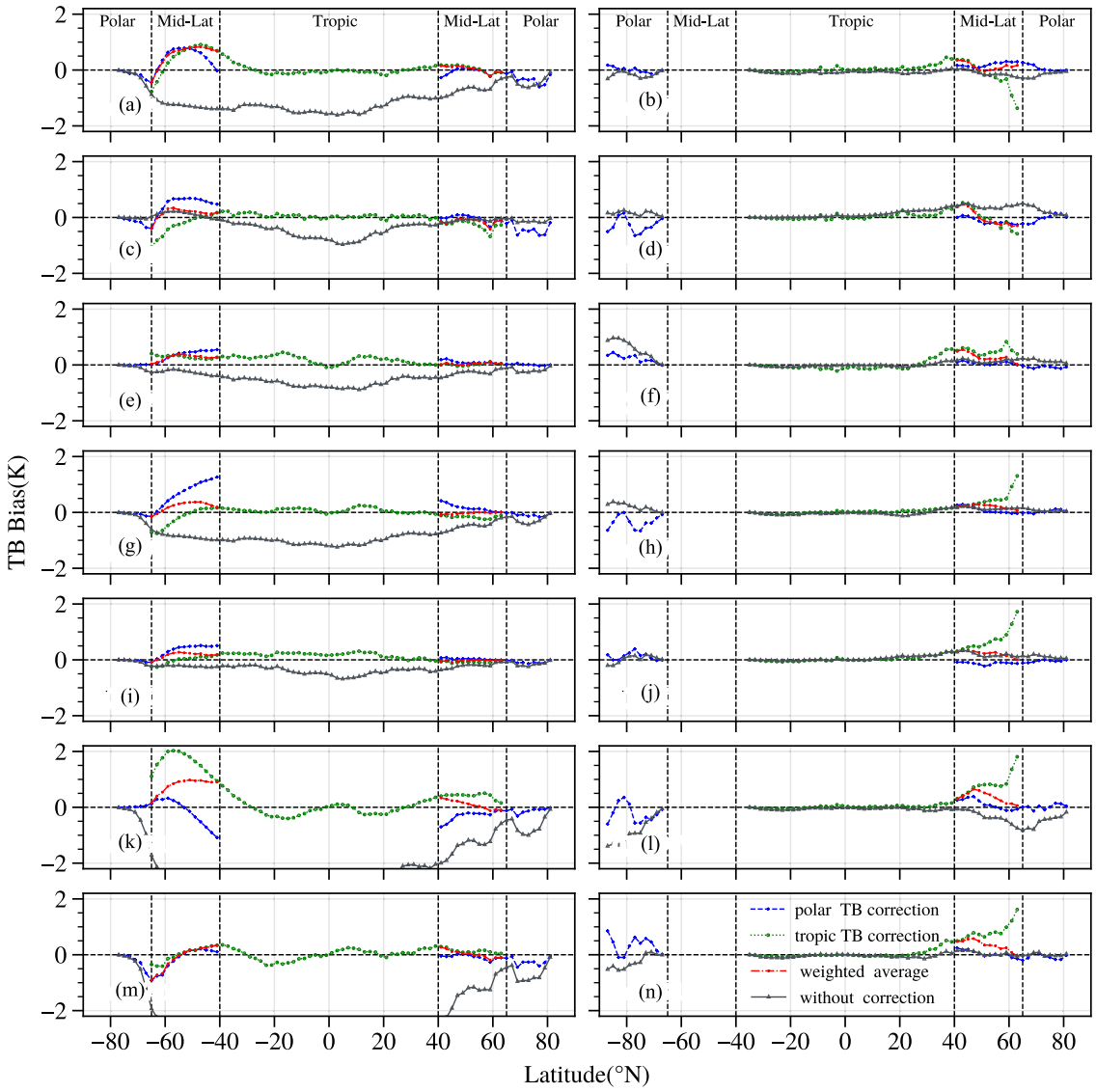

Fig. 5. Latitudinal distribution of TB biases without (gray line) and with intercalibration between F13 SSM/I and F17 SSMIS over (left) global cloud-free ocean and (right) land for all channels. Intercalibration methods include tropical TB correction (green), polar TB correction (blue), and their interpolation (red). The vertical black dotted lines separate different latitudinal regions. Channels are presented from top to bottom as follows. (a) and (b) 19V, (c) and (d) 19H, (e) and (f) 22V, (g) and (h) 37V, (i) and (j) 37H, (k) and (l) 85/91V, and (m) and (n) 85/91H.

measurements. Statistical analysis (see Table III) gives a global mean bias of less than 0.2 K and a standard deviation (STD) of approximately 1 K for all low-frequency channels over both land and ocean after intercalibration. This represents a significant reduction in global mean biases compared to a bias exceeding 3 K before intercalibration. For the 91H channel, the mean TB bias was marginally above 0.2 K after intercalibration. This was likely caused by asynchronous observations of certain unfiltered ice clouds (e.g., deep convective clouds) by the two radiometers, in which high-frequency microwave signals incur significant scattering effect [50].

B. Adjustment of F11 SSM/I

Since there are no overlaps between F11 and the reference F17 (see Table I), the adjustment of the former to the latter is carried out using F13 as the intermediate, which has overlaps with both of them.

First, by employing the same correction approach as described in the previous section, the F11 SSM/I TB was globally adjusted to be consistent with F13 using their SCO matchups as well as matchups with TMI. To evaluate the intercalibration performance, Fig. 7 shows the global distribution of TB biases between F13 and F11 SSM/I before and after intercalibration during their 1999 overlapping period (one year). Table IV lists their mean biases and STDs for global ocean and land, respectively, for all channels. Before intercalibration, channels 19V, 22V, and 37V exhibited large cold biases. After intercalibration, these biases were reduced to around zero for their global means. The magnitudes of these biases are mostly less than 1 K for all channels (more than 90% of the global $1^\circ \times 1^\circ$ grids). On average, the mean biases of all

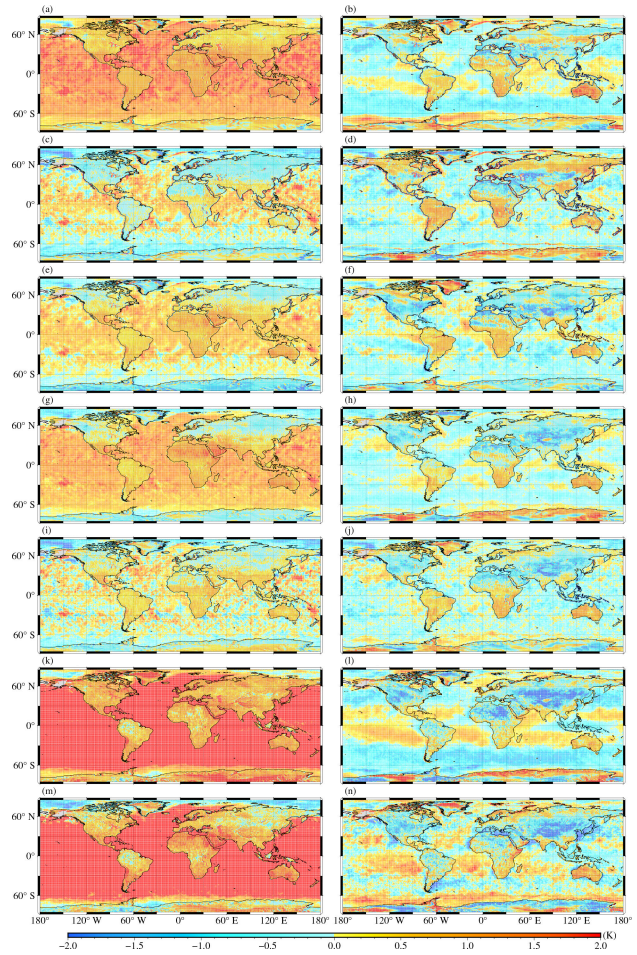

Fig. 6. Global distribution of averaged TB biases between SSMIS on F17 and SSM/I on F13 (left) before and (right) after intercalibration on 1° × 1° grids from October 2008 to September 2009 for all imaging channels. From the top to the bottom: 19V, 19H, 22V, 37V, 37H, 85/91V, and 85/91H. (a) and (b) 19.35V, (c) and (d) 19.35H, (e) and (f) 22.235V, (g) and (h) 37.0V, (i) and (j) 37.0H, (k) and (l) 85.5/91.655V, and (m) and (n) 85.5/91.655H.

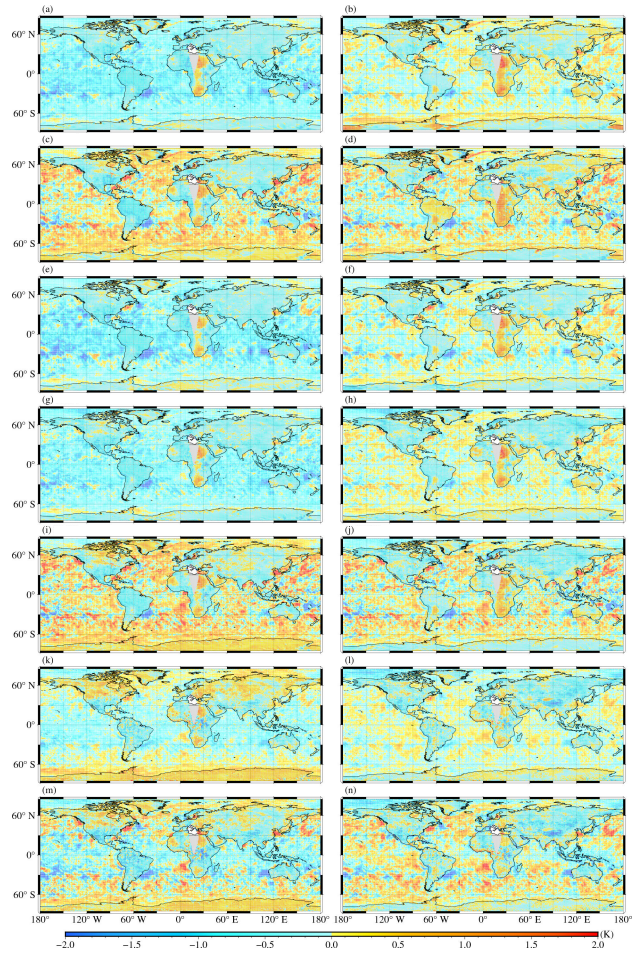

Fig. 7. Similar to Fig. 6, but between SSM/I on F13 and F11 in 1999. (a) and (b) 19.35V, (c) and (d) 19.35H, (e) and (f) 22.235V, (g) and (h) 37.0V, (i) and (j) 37.0H, (k) and (l) 85.5V, and (m) and (n) 85.5H.

TABLE IV

SIMILAR TO TABLE III, BUT BETWEEN SSM/I ON F13 AND F11 IN 1999

	Oceans		Lands	
Channel [GHz]	**Mean[K] Uncal/Cal**	**STD[K] Uncal/Cal**	**Mean[K] Uncal/Cal**	**STD[K] Uncal/Cal**
19.35V	-0.65/-0.04	0.36/0.40	-0.34/-0.06	0.38/0.45
19.35H	0.13/-0.01	0.50/0.68	-0.17/-0.13	0.54/0.47
22.235V	-0.67/-0.05	0.50/0.47	-0.29/-0.16	0.37/0.38
37.0V	-0.63/-0.03	0.33/0.40	-0.37/-0.14	0.39/0.40
37.0H	0.11/-0.05	0.51/0.77	-0.03/-0.19	0.54/0.39
85.5V	-0.25/-0.03	0.43/0.35	0.06/-0.05	0.54/0.51
85.5H	-0.34/-0.22	0.72/0.75	-0.12/-0.08	0.61/0.53

channels were less than 0.2 K after intercalibration with STD below 0.7 K (see Table IV). These results are comparable to or even better than those between F17 SSMIS and the adjusted F13 SSM/I. Overall, the intercalibration process successfully makes the F11 measurements consistent with F13.

The adjusted F11 TBs are considered as the F13-equivalent. The correction relationship and coefficients between the F13 and F17 sensors obtained above are then used to further convert the F13-equivalent to F17-equivalent. Note that it is unfeasible to directly evaluate the consistency between the adjusted F11 SSM/I and the reference F17 SSMIS since there were no overlaps between them. Considering that the correction transformation was effective in adjusting the F13 SSM/I TB in the Tropics using TMI as an intermediate, it is likely that correction results of F11 SSM/I using a similar method are also consistent with TBs from F17 SSMIS. Nevertheless, such consistency will need to be validated against other observations.

IV. FCDR APPLICATION

A direct application of the TB FCDR developed in this study is to retrieve atmospheric and surface variables to construct long-term thematic CDR for climate change research. Before developing such a CDR, we first examine the temporal consistency of the TB FCDRs from the F11, F13, and F17 imagers. Fig. 8 shows time series of the monthly mean TBs for the three satellites and their difference time series over rain-free ocean areas for all the analyzed channels. Here, the monthly mean data were obtained by binning pixel TBs into 1° × 1° latitude–longitude grid cells and averaging them over the monthly intervals. An obvious feature in the monthly TB time series is that all channels show a "two peaks" annual cycle

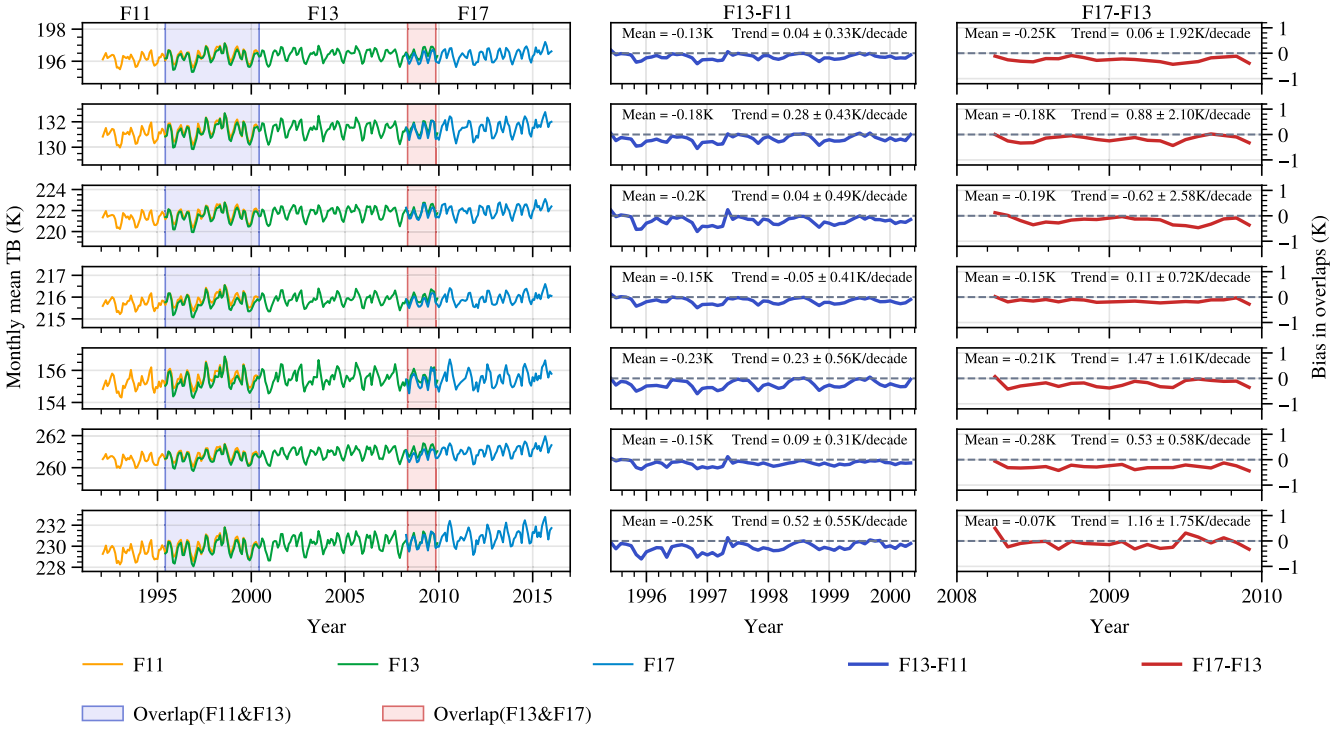

Fig. 8. Monthly mean TB time series for (left) F11, F13, and F17 FCDRs over the cloud-free ocean areas between 60 °S and 60 °N on all imaging channels (from top to bottom: 19V, 19H, 22V, 37V, 37H, 91V, and 91H). Intersatellite difference time series for corresponding channels are shown in the middle figures (F13-F11) and the right figures (F17-F13), respectively. Uncertainties in trend calculations represent 95% confidence intervals with autocorrelation adjustments.

with mean amplitudes from 2 to 4 K, depending on channels. For any of these channels, the two peaks usually occur in February and August, corresponding to boreal winter and summer, respectively. Essentially, these TB cycles in global ocean means reflect an incomplete cancellation effect between the Northern and Southern Hemispheres with opposite phases in the seasonal variations of sea surface temperature and water vapor [58].

To quantitatively evaluate intersatellite drifts after intercalibration, Fig. 8 also listed statistics of means and trends for the difference time series between the satellite pairs. As shown, mean biases in the difference time series were below 0.25 K for all channels and for both satellite pairs between F13 and F11 and between F17 and F13. This is consistent with statistics on their means shown in Tables III and IV, although for different periods of time. Similar to calibration drifts as discussed in Section II, the root cause for these biases could be traced to instrument Level-1 calibration. Zou et al. [57] suggested that errors in blackbody emissivity, sidelobe effect, and instrument nonlinearity could cause calibration biases in microwave radiometer observations. Such biases appeared to exist here in the intersatellite difference time series after removal of hardware differences between satellite pairs. Trend differences between F13 and F11 are less than 0.1 K/decade for most channels which are statistically insignificant. Uncertainties in trend calculations are much larger than the trends themselves due to short overlaps. Note that difference trends between F13 and F17 are sometimes quite large. This is because their overlaps are too short to give meaningful trend values. In any case, these trends are also statistically insignificant. The only difference trend of statistically significant is for channel 85H between F11 and F13. But, this is not a big concern since this channel is not used in CWV retrievals later. Overall, the small and relatively stable intersatellite differences suggested that diurnal drift effect due to their orbital drifts (see Fig. 1) can be ignored and there are smooth transitions in the TB time series during their overlapping periods.

We retrieve the CWV based on the TB FCDRs over the global oceans using a classical algorithm developed by Lojou et al. [59], in which five low-frequency channels (19V, 19H, 22V, 37V, and 37H) were used with a log-linear combination. The Level-2 retrieved CWV is at swath pixel-level for each of the three satellites covering the period from 1991 to 2016. We compared the retrieved CWV with equivalent CWV calculated from radiosonde observations (RAOBs) at standard pressure levels. A total of 37 radiosonde sites on global islands taken from the Integrated Global Radiosonde Archive [60] since December 1991 were selected in the comparison. To minimize mismatch errors, only pixels of the retrieved CWV closest to the RAOB sites were selected in their comparisons. However, if the spatial distances between the selected pixels and the RAOB sites are larger than 10 km, the CWV data pairs were discarded without a comparison. Temporal criteria for the CWV retrievals and RAOB matchups were within 3 h. Fig. 9 shows the density scatter plots and corresponding statistical results between the retrieved CWV CDRs from different satellites and the equivalent RAOB measurements. As seen, the retrieved CWVs are in good agreement with the RAOB observations with a mean deviation less than 0.3 $\mathrm{kg\,m^{-2}}$ and a root mean square error (RMSE) of about 3.0 $\mathrm{kg\,m^{-2}}$,

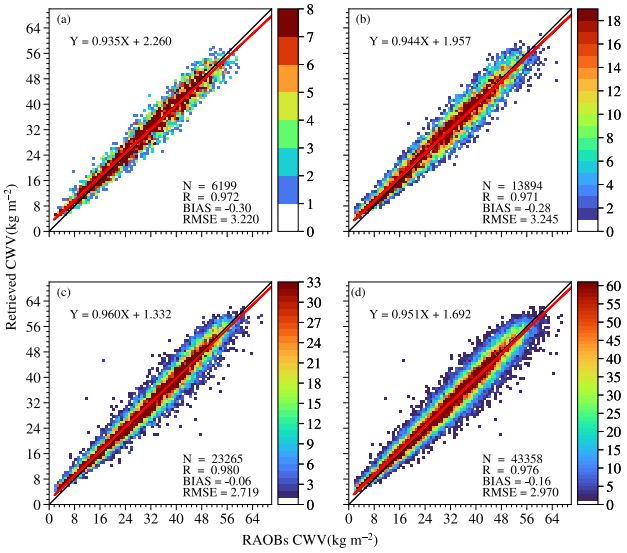

Fig. 9. Density Scatter diagram of the satellite retrieved CWV compared to the equivalent RAOB CWV. The retrieved CWV values are separated into four groups. (a) From F11, (b) from F13, (c) from F17, and (d) combined dataset (ALL). The solid red and black lines represent linear fitting of the data and the diagonal lines, respectively.

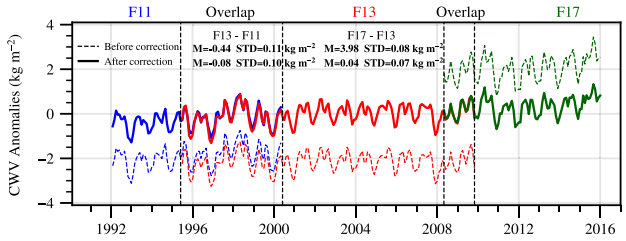

Fig. 10. Monthly anomaly time series of the retrieved CWV for satellites F11, F13, and F17 over the global oceanic rain-free areas from 1992 to 2016 for before and after intercalibration. The thick colored lines represent CWV after intercalibration, while the colored dashed lines represent CWV before intercalibration.

regardless of the satellite instrument used in the retrievals. The overall statistical results are comparable to the accuracy and precision of CWV retrievals from other studies [61], [62]. Also, the similar statistical results across different instruments suggested robustness in the retrieval algorithms as well as consistencies in TBs as their inputs.

The CWV CDR was monthly dataset defined at 0.25° × 0.25° latitude-longitude grid cells. This was done by binning the pixel-level CWVs into the defined grid cells and then averaged over monthly intervals. Fig. 10 shows the gridded CWV time series over the global oceanic rain-free areas for different satellites. Intersatellite differences were close to zero for overlapping satellite pairs, being -0.08 kg m^{-2} for F13-F11 and 0.04 kg m^{-2} for F17-F13 with close to zero bias drifts of statistically insignificant. These intersatellite biases were small but not exactly zero after intercalibration because the intersatellite TB biases were not exactly zero as shown in Fig. 8. To see impact of intercalibration on the CWV retrievals, time series before intercalibration were also shown in Fig. 10. Before intercalibration, intersatellite biases were up to -0.44 kg m^{-2} for F13-F11 and 3.98 kg m^{-2} for F17-F13, respectively. These large intersatellite differences before and after intercalibration would significantly affect long-term trends of the merged CWV time series.

Long-term CWV time series was obtained by merging CWVs from individual satellite retrievals. Before this merging, however, residual intersatellite biases must be removed first. Since intersatellite biases are small and there were no obvious bias drifts between satellite pairs (see Fig. 10), only constant global mean biases calculated from overlapping satellite observations were removed between satellite pairs. Then, the bias-removed CWVs from individual satellites were simply averaged together during their overlapping periods on each grid cell. Fig. 11 depicts the resulting CWV anomaly time series over the global oceans from 1992 to 2016. We examine the performance of the obtained CWV time series by comparing with equivalent CWV computed from the fifth generation European Centre for Medium-Range Weather Forecasts (ECMWF) atmospheric reanalysis (ERA5) monthly gridded (0.25°) climate reanalysis product [63] which is also shown in Fig. 11. It is seen that both time series can well depict the moisture interannual variations with unique annual cycle of "two peaks," similar to those in TBs as described earlier. Also, the satellite retrieved and ERA5 CWVs have high correlations with a coefficient of 0.95 above 99% significant level. Their mean biases are less than 0.5 kg m^{-2} with an RMSE of 0.16 kg m^{-2}.

In addition to the good agreement in short-term variability, both the satellite and reanalysis CWV time series reveal increasing large-scale trends with the former being 0.36 kg m^{-2} (1.464%) per decade and the latter 0.43 kg m^{-2} (1.612%) per decade respectively, only 10% difference. These trend differences were also reflected by their varying differences over time which have a noticeable shift from negative to positive values during the F13 era [see Fig. 11 (bottom)]. It is known that the SSM/I and SSMIS observations had been assimilated into the ERA5 reanalysis system. Variational bias correction was used to remove satellite drifting biases before satellite data were assimilated into the reanalysis system [63]. Considering the very different bias correction schemes used in ERA5 and our satellite retrievals, the CWV trend agreement between the two datasets is considered remarkable. Overall, the satellite retrievals and ERA5 exhibited favorable agreement in both short-term variability and long-term trends, suggesting both of them can be used for climate change research.

Although favorable agreement was achieved for long-term trends between the satellite retrieved CWV and ERA5 climate reanalysis, the comparison is not entirely independent since EAR5 already assimilated the SSM/I and SSMIS data in it. To have a complete independent validation, we compare the satellite retrieved CWV with ground-based observations from the Global Navigation Satellite System (GNSS) [64], [65] network. We select three oceanic stations for the comparison, with station names, respectively, referred to as BRMU (32.37 °N, 64.70 °W), COCO (12.19 °S, 96.83 °E), and DGAR (7.27 °S, 72.37 °E). All the three sites have more than 15 years of overlapping observations with the satellite retrieved CWVs, allowing a reasonably good evaluation of long-term trends. Fig. 12 shows comparisons of time series at these three sites.

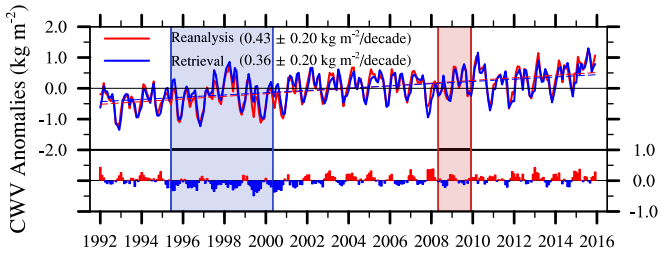

Fig. 11. Monthly anomaly time series of the merged satellite CWV (blue line) and the equivalent CWV from ERA5 reanalysis (red line) over the global oceanic rain-free areas from 1992 to 2016. Long-term trends of the time series are shown as colored dash lines. Anomaly difference time series (reanalysis CWV minus satellite CWV) are shown in the bottom figure with red and blue representing positive and negative values, respectively. Uncertainties in trend calculations represent 95% confidence intervals with autocorrelation adjustments.

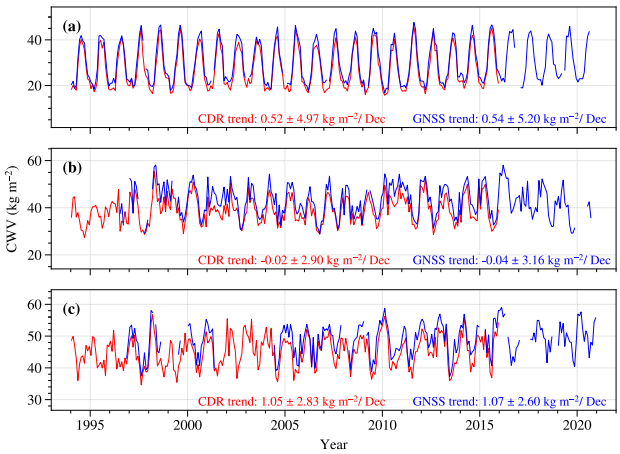

Fig. 12. Monthly time series of intercalibrated satellite CWV (red) and the equivalent GNSS CWV (deep blue) over the three oceanic sites. Long-term trends are calculated over their overlapping periods. (a) BRMU. (b) COCO. (c) DGAR.

All stations demonstrate a high level of consistency between the GNSS and the merged satellite CDR with a trend difference below 0.08%/decade. The correlation coefficients for their monthly time series are high, being 0.991, 0.948, and 0.939 for the BRMU, COCO, and DGAR stations, respectively. These comparisons demonstrate the merit of intercalibration that has resulted in CWV trend consistent with overlapping GNSS observations.

V. Conclusion

We developed a continuous and highly consistent TB FCDR for up to 30 years from December 1991 to December 2021 using measurements by SSM/I instrument onboard F11 and F13 and SSMIS instrument onboard F17. In this process, the F17 SSMIS observations were used as a reference while TBs from the SSM/I's onboard F11 and F13 were converted to SSMIS-equivalent TB by intersensor bias correction. Biases removed included a systematic bias drift over time for all sensors and hardware differences between different sensors. A VCR approach was used to remove the systematic bias drifts and a PCA method was used for removing hardware differences. The PCA approach was applied to separate geographical regions including the tropics, midlatitudes, and polar regions for the best effect of bias correction. After intersensor recalibration, mean biases between any two radiometers have been reduced to less than 0.2 K with an STD of 1.2 K for almost all channels over both land and ocean. The small biases were also relatively stable for all analyzed channels during the overlapping periods between satellite pairs, suggesting temporal consistency in the resultant TB FCDRs on pixel-level.

The consistent FCDR was applied to develop a long-term atmospheric CWV CDR over 25 years from 1992 to 2016. Comparison with ground-based RAOB observations, indicates that the CWV CDR has achieved an accuracy of 0.3 kg m^{-2} with an RMSE of about 3.0 kg m^{-2} for all the three satellites. Interannual variability in the CWV time series agreed well with the ERA5 reanalysis with a high correlation coefficient of 0.95 and low RMSE of 0.16 kg m^{-2}. The long-term trends from the CWV CDR also agreed well with those observed from GNSS stations over the ocean. These results suggest that the CWV CDR is suitable for climate change research. They also suggest the application potential of the TB FCDR as the fundamental observational dataset for climate research.

It should be emphasized that the correction approaches proposed in this study for hardware differences between instruments may also be applied for obtaining calibration consistency and TB FCDR of any PMW radiometers on other satellites with longer observation periods and higher sampling frequency. This provides an effective tool for FCDR development which would further help the CDR development for understanding long-term changes in the climate system.

Acknowledgment

The authors are greatly appreciative of the GPM Intersatellite Calibration (X-CAL) Working Group for providing the recalibrated SSM/I, SSMIS, and TMI TB datasets. They would thank the three anonymous reviewers for their invaluable and insightful comments. Their constructive comments have greatly helped improve the quality of this manuscript.

For Cheng-Zhi Zou, the views, opinions, and findings contained in this report are those of the authors and should not be construed as an official NOAA or U.S. Government position, policy, or decision.

References

[1] F. J. Wentz, "A well-calibrated ocean algorithm for special sensor microwave/imager," *J. Geophys. Res., Oceans*, vol. 102, no. 4, pp. 8703–8718, Apr. 1997, doi: 10.1029/96JC01751.

[2] J. Wen, Z. Su and Y. Ma, "Determination of land surface temperature and soil moisture from tropical rainfall measuring mission/microwave imager remote sensing data," *J. Geophys. Res.*, vol. 108, no. D2, pp. 4038–4047, Jan. 2003, doi: 10.1029/2002JD002176.

[3] T. R. H. Holmes, R. A. M. De Jeu, M. Owe, and A. J. Dolman, "Land Surface Temperature from Ka band (37 GHz) passive microwave observations," *J. Geophys. Res.*, vol. 114, no. 4, 2009, Art. no. D04113, doi: 10.1029/2008JD010257.

[4] Y. Wang, Y. Fu, G. Liu, Q. Liu, and L. Sun, "A new water vapor algorithm for TRMM microwave imager (TMI) measurements based on a log linear relationship," *J. Geophys. Res.*, vol. 114, no. 21, pp. D21304-1–D21304-12, 2009, doi: 10.1029/2008JD011057.

[5] J. P. Hollinger, "DMSP SSM/I; Current status," in *Proc. 10th Annu. Int. Symp. Geosci. Remote Sens.*, 1990, p. 201.

[6] J. J. Bommarito, "DMSP special sensor microwave imager sounder (SSMIS)," *Proc. SPIE*, vol. 1935, pp. 230–238, Aug. 1993. [Online]. Available: https://api.semanticscholar.org/CorpusID:121472936

[7] D. B. Kunkee et al., "Design and evaluation of the first special sensor microwave imager/sounder," *IEEE Trans. Geosci. Remote Sens.*, vol. 46, no. 4, pp. 863–883, Apr. 2008.

[8] R. A. Kroodsma, W. Berg, and T. T. Wilheit, "Special sensor microwave imager/sounder updates for the global precipitation measurement V07 data suite," *IEEE Trans. Geosci. Remote Sens.*, vol. 60, 2022, Art. no. 5303511.

[9] J. C. Alishouse, S. A. Snyder, J. Vongsathorn, and R. R. Ferraro, "Determination of oceanic total precipitable water from the SSM/I," *IEEE Trans. Geosci. Remote Sens.*, vol. 28, no. 5, pp. 811–816, Sep. 1990.

[10] P. Schluessel and W. J. Emery, "Atmospheric water vapour over oceans from SSM/I measurements," *Int. J. Remote Sens.*, vol. 11, no. 5, pp. 753–766, May 1990, doi: 10.1080/01431169008955055.

[11] J. Schulz, P. Schluessel, and H. Grassl, "Water vapour in the atmospheric boundary layer over oceans from SSM/I measurements," *Int. J. Remote Sens.*, vol. 14, no. 15, pp. 2773–2789, Oct. 1993, doi: 10.1080/01431169308904308.

[12] F. Weng and N. C. Grody, "Retrieval of cloud liquid water using the special sensor microwave imager (SSM/I)," *J. Geophys. Res., Atmos.*, vol. 99, no. 12, pp. 25535–25551, 1994, doi: 10.1029/94JD02304.

[13] R. R. Ferraro and G. F. Marks, "The development of SSM/I rain-rate retrieval algorithms using ground-based radar measurements," *J. Atmos. Ocean. Technol.*, vol. 12, no. 4, pp. 755–770, Aug. 1995. [Online]. Available: https://journals.ametsoc.org/view/journals/atot/12/4/1520-0426_1995_012_0755tdosrr20co2.xml

[14] F. J. Wentz and R. W. Spencer, "SSM/I rain retrievals within a unified all-weather ocean algorithm," *J. Atmos. Sci.*, vol. 55, no. 9, pp. 1613–1627, May 1998. [Online]. Available: https://journals.ametsoc.org/view/journals/atsc/55/9/1520-0469_1998_055_1613sirrwa2.0.co2.xml

[15] P. Chylek, C. C. Borel, W. Clodius, P. A. Pope, and A. P. Rodger, "Satellite-based columnar water vapor retrieval with the multi-spectral thermal imager (MTI)," *IEEE Trans. Geosci. Remote Sens.*, vol. 41, no. 12, pp. 2767–2770, Dec. 2003.

[16] M. N. Deeter, "A new satellite retrieval method for precipitable water vapor over land and ocean," *Geophys. Res. Lett.*, vol. 34, no. 2, pp. 1–20, 2007, doi: 10.1029/2006GL028019.

[17] C. D. Kummerow et al., "The evolution of the Goddard profiling algorithm to a fully parametric scheme," *J. Atmos. Ocean. Technol.*, vol. 32, no. 12, pp. 2265–2280, Dec. 2015. [Online]. Available: https://journals.ametsoc.org/view/journals/atot/32/12/jtech-d-15-0039_1.xml

[18] M. J. McFarland, R. L. Miller, and C. M. U. Neale, "Land Surface Temperature derived from the SSM/I passive microwave brightness temperatures," *IEEE Trans. Geosci. Remote Sens.*, vol. 28, no. 5, pp. 839–845, Sep. 1990.

[19] R. Atlas, R. N. Hoffman, S. C. Bloom, J. C. Jusem, and J. Ardizzone, "A multiyear global surface wind velocity dataset using SSM/I wind observations," *Bull. Amer. Meteorological Soc.*, vol. 77, no. 5, pp. 869–882, May 1996. [Online]. Available: https://journals.ametsoc.org/view/journals/bams/77/5/1520-0477_1996_077_0869_amgswv_2_0_co_2.xml

[20] S. Paloscia, G. Macelloni, E. Santi, and T. Koike, "A multifrequency algorithm for the retrieval of soil moisture on a large scale using microwave data from SMMR and SSM/I satellites," *IEEE Trans. Geosci. Remote Sens.*, vol. 39, no. 8, pp. 1655–1661, 2001.

[21] C. Prigent, C. Jimenez, and F. Aires, "Toward 'all weather' long record, and real-time Land Surface Temperature retrievals from microwave satellite observations," *J. Geophys. Res., Atmos.*, vol. 121, no. 10, pp. 5699–5717, May 2016, doi: 10.1002/2015JD024402.

[22] P. Yao et al., "A long term global daily soil moisture dataset derived from AMSR-E and AMSR2 (2002–2019)," *Sci. Data*, vol. 8, no. 1, p. 143, May 2021, doi: 10.1038/s41597-021-00925-8.

[23] M. C. Colton and G. A. Poe, "Intersensor calibration of DMSP SSM/I's: F-8 to F-14, 1987–1997," *IEEE Trans. Geosci. Remote Sens.*, vol. 37, no. 1, pp. 418–439, Jan. 1999.

[24] S. Yang, F. Weng, B. Yan, N. Sun, and M. Goldberg, "Special sensor microwave imager (SSM/I) intersensor calibration using a simultaneous conical overpass technique," *J. Appl. Meteorol. Climatol.*, vol. 50, no. 1, pp. 77–95, Jan. 2011. [Online]. Available: https://journals.ametsoc.org/view/journals/apme/50/1/2010jamc2271.1.xml

[25] M. R. P. Sapiano, W. K. Berg, D. S. McKague, and C. D. Kummerow, "Toward an intercalibrated fundamental climate data record of the SSM/I sensors," *IEEE Trans. Geosci. Remote Sens.*, vol. 51, no. 3, pp. 1492–1503, Mar. 2013.

[26] C. S. Ruf, "Detection of calibration drifts in spaceborne microwave radiometers using a vicarious cold reference," *IEEE Trans. Geosci. Remote Sens.*, vol. 38, no. 1, pp. 44–52, Jan. 2000.

[27] W. Berg et al., "Intercalibration of the GPM microwave radiometer constellation," *J. Atmos. Ocean. Technol.*, vol. 33, no. 12, pp. 2639–2654, Dec. 2016. [Online]. Available: https://journals.ametsoc.org/view/journals/atot/33/12/jtech-d-16-0100_1.xml

[28] F. Wentz. (2012). *SSM/I Version-7 Calibration Report*. [Online]. Available: https://api.semanticscholar.org/CorpusID:130515710

[29] F. J. Wentz and D. Draper, "On-orbit absolute calibration of the global precipitation measurement microwave imager," *J. Atmos. Ocean. Technol.*, vol. 33, no. 7, pp. 1393–1412, Jul. 2016. [Online]. Available: https://journals.ametsoc.org/view/journals/atot/33/7/jtech-d-15-0212_1.xml

[30] K. Fennig, M. Schröder, A. Andersson, and R. Hollmann, "A fundamental climate data record of SMMR, SSM/I, and SSMIS brightness temperatures," *Earth Syst. Sci. Data*, vol. 12, no. 1, pp. 647–681, Mar. 2020. [Online]. Available: https://essd.copernicus.org/articles/12/647/2020/

[31] B. Wu et al., "A fundamental climate data record derived from AMSR-E, MWRI, and AMSR2," *IEEE Trans. Geosci. Remote Sens.*, vol. 58, no. 8, pp. 5450–5461, Aug. 2020.

[32] J. P. Hollinger, J. L. Peirce, and G. A. Poe, "SSM/I instrument evaluation," *IEEE Trans. Geosci. Remote Sens.*, vol. 28, no. 5, pp. 781–790, Sep. 1990.

[33] G. S. Elsaesser and C. D. Kummerow, "Toward a fully parametric retrieval of the nonraining parameters over the global oceans," *J. Appl. Meteorol. Climatol.*, vol. 47, no. 6, pp. 1599–1618, Jun. 2008. [Online]. Available: https://journals.ametsoc.org/view/journals/apme/47/6/2007jamc1712.1.xml

[34] W. N. Meier, S. J. S. Khalsa, and M. H. Savoie, "Intersensor calibration between F-13 SSM/I and F-17 SSMIS near-real-time sea ice estimates," *IEEE Trans. Geosci. Remote Sens.*, vol. 49, no. 9, pp. 3343–3349, Sep. 2011.

[35] D. J. Cavalieri, C. L. Parkinson, N. DiGirolamo, and A. Ivanoff, "Intersensor calibration between F13 SSMI and F17 SSMIS for global sea ice data records," *IEEE Geosci. Remote Sens. Lett.*, vol. 9, no. 2, pp. 233–236, Mar. 2012.

[36] T. Lavergne et al., "Version 2 of the EUMETSAT OSI SAF and ESA CCI sea-ice concentration climate data records," *Cryosphere*, vol. 13, no. 1, pp. 49–78, 2019. [Online]. Available: https://tc.copernicus.org/articles/13/49/2019/

[37] X. D. Wang, K. Zhang, D. hui Shangguan, and Y. H. Wang, "Spatio-temporal changes of snowmelt in Greenland ice sheet based on SSM/I (SSMIS) data (1988–2016)," *Indian J. Geo-Marine Sci.*, vol. 50, no. 5, pp. 359–365, 2021. [Online]. Available: https://api.semanticscholar.org/CorpusID:252746032

[38] P. Colosio, M. Tedesco, R. Ranzi, and X. Fettweis, "Surface melting over the Greenland ice sheet derived from enhanced resolution passive microwave brightness temperatures (1979–2019)," *Cryosphere*, vol. 15, no. 6, pp. 2623–2646, Jun. 2021. [Online]. Available: https://tc.copernicus.org/articles/15/2623/2021/

[39] L. Jiang et al., "Daily snow water equivalent product with SMMR, SSM/I and SSMIS from 1980 to 2020 over China," *Big Earth Data*, vol. 6, no. 4, pp. 420–434, Oct. 2022, doi: 10.1080/20964471.2022.2032998.

[40] F. J. Turk, Z. S. Haddad, and Y. You, "Principal components of multifrequency microwave land surface emissivities. Part I: Estimation under clear and precipitating conditions," *J. Hydrometeorol.*, vol. 15, no. 1, pp. 3–19, Feb. 2014. [Online]. Available: https://journals.ametsoc.org/view/journals/hydr/15/1/jhm-d-13-08_1.xml

[41] W. Berg, R. Kroodsma, C. Kummerow, and D. McKague, "Fundamental climate data records of microwave brightness temperatures," *Remote Sens.*, vol. 10, no. 8, p. 1306, Aug. 2018. [Online]. Available: https://www.mdpi.com/2072-4292/10/8/1306

[42] W. K. Berg. *GPM SSMI F11 Common Calibrated Brightness Temperatures L1C 1.5 Hours 12 km V06*, Greenbelt, MD, USA, Goddard Earth Sciences Data and Information Services Center (GES DISC) Std., 2018, doi: 10.5067/GPM/SSMI/F11/1C/06.

[43] W. K. Berg. *GPM SSMI F13 Common Calibrated Brightness Temperatures L1C 1.5 hours 12 km V06*, Greenbelt, MD, USA, Goddard Earth Sciences Data and Information Services Center (GES DISC) Std., 2018, doi: 10.5067/GPM/SSMI/F13/1C/06.

[44] W. K. Berg. *GPM SSMIS F17 Common Calibrated Brightness Temperatures L1C 1.5 hours 12 km V05*, Greenbelt, MD, USA, Goddard Earth Sciences Data and Information Services Center (GES DISC) Std., 2016, doi: 10.5067/GPM/SSMIS/F17/1C/05.

[45] Z. Sharifnezhad, H. Norouzi, S. Prakash, R. Blake, and R. Khanbilvardi, "Diurnal cycle of passive microwave brightness temperatures over land at a global scale," *Remote Sens.*, vol. 13, no. 4, p. 817, Feb. 2021. [Online]. Available: https://www.mdpi.com/2072-4292/13/4/817
[46] S.-M. Lee, B.-J. Sohn, and C. Kummerow, "Long-term Arctic snow/ice interface temperature from special sensor for microwave imager measurements," *Remote Sens.*, vol. 10, no. 11, p. 1795, Nov. 2018. [Online]. Available: https://api.semanticscholar.org/CorpusID:56482021
[47] H. Liu, Z. Wei, and X. Nie, "Assessing the relationship between freshwater flux and sea surface salinity," *Remote Sens.*, vol. 14, no. 9, p. 2149, Apr. 2022.
[48] W. Yang, H. Meng, R. R. Ferraro, and Y. Chen, "Inter-Calibration of AMSU-A Window Channelss," *Remote Sens.*, vol. 12, no. 18, p. 2988, 2020. [Online]. Available: https://www.mdpi.com/2072-4292/12/18/2988
[49] A. P. Stogryn, C. T. Butler, and T. J. Bartolac, "Ocean surface wind retrievals from special sensor microwave imager data with neural networks," *J. Geophys. Res.*, vol. 99, no. C1, pp. 981–984, 1994, doi: 10.1029/93JC03042.
[50] R. A. Kroodsma, D. S. McKague, and C. S. Ruf, "Extension of vicarious cold calibration to 85–92 GHz for spaceborne microwave radiometers," *IEEE Trans. Geosci. Remote Sens.*, vol. 51, no. 9, pp. 4743–4751, Sep. 2013.
[51] W. K. Berg. *GPM TMI TRMM Common Calibrated Brightness Temperatures L1C 1.5 hours 13 km V05*, Greenbelt, MD, USA, Goddard Earth Sciences Data and Information Services Center (GES DISC) Std., 2016, doi: 10.5067/GPM/TMI/TRMM/1C/05.
[52] T. R. Loveland and A. S. Belward, "The IGBP-DIS global 1 km land cover data set, DISCover: First results," *Int. J. Remote Sens.*, vol. 18, no. 15, pp. 3289–3295, Oct. 1997, doi: 10.1080/014311697217099.
[53] D. S.-M. Friedl. *MCD12C1 MODIS/Terra+Aqua Land Cover Type Yearly L3 Global 0.05Deg CMG V006*, NASA EOSDIS Land Processes Distributed Active Archive Center Std., 2015, doi: 10.5067/MODIS/MCD12C1.006.
[54] Z. Liu, C.-L. Shie, A. Li, and D. Meyer, "NASA global satellite and model data products and services for tropical meteorology and climatology," *Remote Sens.*, vol. 12, no. 17, p. 2821, Aug. 2020. [Online]. Available: https://www.mdpi.com/2072-4292/12/17/2821
[55] R. A. Kroodsma, D. S. McKague, and C. S. Ruf, "Vicarious cold calibration for conical scanning microwave imagers," *IEEE Trans. Geosci. Remote Sens.*, vol. 55, no. 2, pp. 816–827, Feb. 2017.
[56] X. Xie, K. Dong, W. Yu, W. Meng, and S. Gu, "In-orbit calibration of FengYun-3C microwave radiation imager: Nonlinearity correction," *IEEE Trans. Geosci. Remote Sens.*, vol. 59, no. 9, pp. 7618–7626, Sep. 2021.
[57] C. Zou, H. Xu, X. Hao, and Q. Liu, "Mid-tropospheric layer temperature record derived from satellite microwave sounder observations with backward merging approach," *J. Geophys. Res., Atmos.*, vol. 128, no. 6, Mar. 2023, Art. no. e2022JD037472, doi: 10.1029/2022JD037472.
[58] G. Chen, "A 10-yr climatology of oceanic water vapor derived from the TOPEX microwave radiometer," *J. Climate*, vol. 17, no. 13, pp. 2541–2557, Jul. 2004. [Online]. Available: https://journals.ametsoc.org/view/journals/clim/17/13/1520-0442_2004_017_2541_aycoow_2.0.co_2.xml
[59] J.-Y. Lojou, R. Bernard, and L. Eymard, "A simple method for testing brightness temperatures from satellite microwave radiometers," *J. Atmos. Ocean. Technol.*, vol. 11, no. 2, pp. 387–400, Apr. 1994. [Online]. Available: https://journals.ametsoc.org/view/journals/atot/11/2/1520-0426_1994_011_0387_asmftb_2_0_co_2.xml
[60] I. Durre, R. S. Vose, and D. B. Wuertz, "Overview of the integrated global radiosonde archive," *J. Climate*, vol. 19, no. 1, pp. 53–68, Jan. 2006. [Online]. Available: https://journals.ametsoc.org/view/journals/clim/19/1/jcli3594.1.xml
[61] S.-A. Boukabara, K. Garrett, and W. Chen, "Global coverage of total precipitable water using a microwave variational algorithm," *IEEE Trans. Geosci. Remote Sens.*, vol. 48, no. 10, pp. 3608–3621, Oct. 2010.
[62] J.-P. Guan, Y.-T. Yin, L.-F. Zhang, J.-N. Wang, and M.-Y. Zhang, "Comparison analysis of total precipitable water of satellite-borne microwave radiometer retrievals and island radiosondes," *Atmosphere*, vol. 10, no. 7, p. 390, Jul. 2019.
[63] H. Hersbach et al., "The ERA5 global reanalysis," *Quart. J. Roy. Meteorological Soc.*, vol. 146, no. 730, pp. 1999–2049, Jul. 2020, doi: 10.1002/qj.3803.
[64] O. Bock, *Global GNSS Integrated Water Vapour Data, 1994–2020*, AERIS Std., 2020, doi: 10.25326/68.
[65] R. J. H. Dunn et al., "Global climate," *Bull. Amer. Meteorological Soc.*, vol. 103, no. 8, pp. 11–142, 2022 [Online]. Available: https://journals.ametsoc.org/view/journals/bams/103/8/BAMS-D-22-0092.1.xml

Shi Liu received the B.S. degree from the University of Science and Technology of China, Hefei, China, in 2018, where he is currently pursuing the Ph.D. degree with the School of Earth and Space Sciences.

His research interests include the intercalibration of satellite passive microwave observations and climate research.

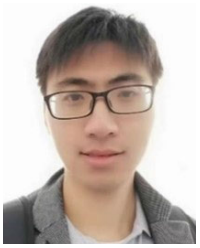

Banghai Wu received the B.S. degree in atmospheric science from the University of Science and Technology of China (USTC), Hefei, China, in 2016, where he is currently pursuing the Ph.D. degree.

His main research interests include satellite remote sensing and climate change.

Cheng-Zhi Zou received the B.S. degree in atmospheric science from the University of Science and Technology of China, Hefei, China, in 1982, the M.S. degree in atmospheric science from the Institute of Atmospheric Physics, Chinese Academy of Sciences, Beijing, China, in 1985, and the Ph.D. degree in climatology from The University of Oklahoma, Norman, OK, USA, in 1995.

He is currently a Physical Scientist with the Center for Satellite Applications and Research, National Environmental Satellite, Data, and Information Service, National Oceanic and Atmospheric Administration, College Park, MD, USA. His research interests include satellite climatology, including satellite instrument calibration and recalibration, the development of climate data records using satellite observations, and the use of satellite observations in global change monitoring.

Yu Wang received the B.S., M.S., and Ph.D. degrees in atmospheric science from the University of Science and Technology of China, Hefei, China, in 2000, 2003, and 2008, respectively.

He is currently a Professor with the School of Earth and Space Sciences and the Hefei National Laboratory, University of Science and Technology of China, and also with the Chinese Academy of Sciences (CAS) Center for Excellence in Comparative Planetology. His research interests include microwave remote sensing and the interactions of aerosol, cloud, and precipitation.